Songklanakarin J. Sci. Technol.
45 (3), 442–450, May – Jun. 2023

http://www.sjst.psu.ac.th

Original Article

Investigation on microstructure and mechanical properties of 17-4PH stainless steels fabricated by materials extrusion additive manufacturing

Pasut Promsuwan[1], Ruangdaj Tongsri[2], Pruet Kowitwarangkul[1*], Patiparn Ninpetch[1], and Thotsaphon Threrujirapapong[3]

[1] *The Sirindhorn International Thai-German Graduate School of Engineering, King Mongkut's University of Technology North Bangkok, Bang Sue, Bangkok, 10800 Thailand*

[2] *National Metal and Materials Technology Center (MTEC), National Science and Technology Development Agency (NSTDA), Khlong Luang, Pathum Thani, 12120, Thailand*

[3] *Faculty of Engineering, King Mongkut's University of Technology North Bangkok, Bang Sue, Bangkok, 10800 Thailand*

Received: 29 November 2022; Revised: 17 February 2023; Accepted: 13 May 2023

Abstract

Materials extrusion additive manufacturing (MEAM) is currently attracting various industries as a modern manufacturing process that can produce complex parts with a lower cost than those of other additive manufacturing processes. In this study, the microstructure and mechanical properties of additively manufactured and wrought 17-4PH stainless steels as parts in original condition and in heat-treated under H900 condition were compared. The original specimen comprised martensite and δ-ferrite. After solution treatment, the δ-ferrite phase exhibited clear growth in martensite matrix. The precipitation strengthening due to aging treatment was evidenced by increases in tensile strength and hardness. Furthermore, strength coefficient (K) and strain hardening exponent (n) obtained from experiment were used as input data for simulation of tensile test. The simulation results for all specimens are in agreement with the experimental results. The findings from the simulation results are expected to be useful for prediction of mechanical behavior of complex parts fabricated by MEAM process.

Keywords: additive manufacturing, materials extrusion additive manufacturing, 17-4PH stainless steel, heat treatment, precipitation strengthening, finite element method

1. Introduction

Additive manufacturing (AM) processes have been widely used to produce complex shaped parts that are difficult to manufacture using traditional manufacturing processes. An AM type of process is novel technology for fabricating parts by adding material layer-by-layer, controlled by a computer-aided design (CAD) file (Milner *et al.*, 2021; Herzog, Seyda, Wycisk, & Reutzel, 2016). Such process can build components from various materials such as metal, polymer, ceramic, composite, or biomaterial (Sookchanchai, Promoppatum & Uthaisangsuk, 2022). Metal AM processes can be classified into two groups based on the energy source: 1) beam-based processes, and 2) beamless processes. The selective laser melting (SLM), and direct energy deposition (DED) are famous beam-based processes. The most popular beamless processes, in contrast, are binder jetting (BJ), materials jetting, and materials extrusion additive manufacturing (MEAM) (Pant, Nagdeve, Kumar, & Moona, 2021). Additionally, numerous metallic materials including stainless steel, tool steel, titanium alloys, and superalloys can be used as raw materials for metal AM processing.

Over the past decades, there have been many research studies on metal AM by using experimental and

*Corresponding author
Email address: pruet.k@tggs.kmutnb.ac.th

numerical methods. Most of the studies have focused on the effects of processing parameters on physical properties, mechanical properties, and microstructure. Table 1 presents the previous studies on metal AM processes.

Furthermore, additional exemplary research studies on metal AM processes have been reported in review articles (Herzog *et al.*, 2016; Milner *et al.*, 2021; Ninpetch, Kowitwarangkul, Mahathanabodee, Chalermkarnnon, & Ratanadecho, 2020). From the literature review, it was found that very few studies on the MEAM process had been published. Therefore, this research will focus on the MEAM, which is a combination of two technologies. One is the fused deposition modeling (FDM), which involves a moving extruder building a 3D part layer-by-layer with an extruded thermoplastic filament. The FDM process is widely used and can greatly reduce production costs. The other technology is metal injection molding (MIM), a powder metallurgical technique in which binder is removed and metal particles are sintered together at temperatures below their melting points (Abe *et al.*, 2021; Kurose *et al.*, 2020). Generally, the MEAM process is divided into 4 steps. In step 1, the raw materials are prepared in the form of wire (or rod), also known as feedstock, which consists of metal powder particles and a thermoplastic organic binder. Step 2 is the fabrication of workpieces, in which the feedstock is extruded and stacked layer-by-layer in the Z-direction (building direction) into 3D parts, known as green parts. Step 3 is the removal of binder (debinding) by soaking the green parts in a solvent to get rid of the waxy binder. After that, the removal of polymeric binders is done by thermal debinding. Step 4 is sintering, in which metal powder particles are bonded together, giving strength to the 3D parts. Metal powder compacts are converted into coherent solids by sintering at temperatures below their melting point (Rahman, 2018). As mentioned earlier, the green parts obtained from printing by MEAM must be sintered to increase the strength of parts. As a result, the microstructure and mechanical properties of the built part are different from those induced by conventional processing, such as hot rolling. Therefore, understanding the microstructure and mechanical properties of the part produced by MEAM are essential and can lead to suitable design of metal parts that prevents their premature failure.

The aims of this study were to investigate microstructure and mechanical properties, e.g. tensile strength and hardness of 17-4PH stainless steel when additively manufactured (AM) and also of wrought parts as original and as heat-treated under the H900 condition. The tensile strength was compared with the results for MIM parts from literature. The strength coefficient (K) and strain hardening exponent (n) were calculated from stress-strain curve determined experimentally. Afterwards, numerical simulation with the finite element method (FEM) was implemented using the K and n values to investigate the mechanical behavior of the specimen. The simulation results of tensile test were validated against the experimental results. The findings from the simulation results are expected to be useful for predicting mechanical behavior of additively manufactured parts fabricated by the MEAM process. This study also includes one case study of the simulation of a bevel gear using the properties of MEAM specimens.

Table 1. Previous studies on metal AM processes

Process	Material	Studies
SLM	316L	(Mussatto *et al.*, 2022; Pitrmuc *et al.*, 2022; Pagac *et al.*, 2021)
	17-4PH	(Li *et al.*, 2022; Sabooni *et al.*, 2021; Sun, Hebert, & Aindow, 2018)
	Ti-6Al-4V	(Ninpetch *et al.*, 2022; Zhang *et al.*, 2019)
	H13	(Ninpetch, Chalermkarnnon, & Kowitwarangkul, 2022; Ninectch, Kowitwarangkul, Mahathanabodee, Chalermkarnnon, & Rattanadecho, 2021)
BJ	316L	(Zhang *et al.*, 2021; Meenashisundaram *et al.* 2020; Oropeza, & Hart, 2021; Mirzababaei, Paul, & Pasebani, 2020)
	17-4PH	(Huber, Stich, & Fischer, 2022)
	Ti-6Al-4V	(Wheat, Vlasea, Hinebaugh, & Metcalfe, 2018)
	H13	(Nandwana, Kannan, & Siddel, 2021)
DED	316L	(Kumaran, Senthilkumar, Panicke, & Shishir, 2021; Farshidianfar, Khodabakhshi, Khajepour, & Gerlich, 2021; Saboori *et al.*, 2019; Haley *et al.*, 2016)
	Ti-6Al-4V	(Chen *et al.*, 2021; Gorunov, A.I., 2020; Heigel, Michaleris, & Reutzel, 2015)
MEAM	316L	(Kurose *et al.*, 2020)
	17-4PH	(Abe *et al.*, 2021)

2. Materials and Methods

2.1 Materials

The material used for this experiment is 17-4PH stainless steel grade. The material is divided into two types. The first type is a material for AM specimens, which is composed of 17-4PH stainless steel particles and thermoplastic organic binder, obtained from Desktop Metal. It was used in the printing process. The second group is wrought 17-4PH stainless steel specimens received as hot rolled plate and through annealed parts. The chemical compositions of the 17-4PH stainless steel samples were determined as given in Table 2.

Table 2. Chemical compositions of 17-4PH stainless steel as hot rolled plates and as AM feedstock

17-4PH stainless steel	Chemical composition (%wt.)						
	Fe	Cr	Ni	Cu	C	Mn	Nb + Ta
AM	70.98- 77.28	15.5-17.5	3-5	3-5	0.07(max)	1.0 (max)	0.15-0.45
Wrought	76.18	15.32	4.5	3.36	0.034	0.59	0.02

2.2 Metal 3D printing process

The samples of AM specimens were produced using the studio system of Desktop Metal, which is a MEAM process. The system consists of a 3D printer, debinding machine, and sintering furnace. As mentioned above, the green part obtained from printing requires debinding and sintering to increase its strength. The printing parameters applied in this study included 0.4 mm nozzle dimeter, 165 ºC nozzle temperature, 50 ºC chamber temperature, 65 ºC stage temperature, 8 cc/hr printing rate, and 4.5 mm layer thickness. The green parts in the study were built in horizontal direction as illustrated in Figures 1 (b) and (c). After printing, the green specimens were soaked in solvent for 2 hours to remove the wax. Then, the green parts were subjected to thermal debinding at 600 ºC for 2 hours under a nitrogen atmosphere to remove the organic binder. Thereafter, the brown specimens were sintered at 1280 ºC for 2 hours in argon atmosphere. Thermal debinding and sintering were carried out continuously in the same vacuum furnace. The sintered specimens were cooled in the furnace. The studio system of Desktop Metal at Thaisakol Group Co., Ltd., is shown in Figure 1.

Figure 1. (a) The studio system of Desktop Metal at Thaisakol Group Co., Ltd., (b) build direction is horizontal, and (c) 3D printed specimen after sintering

2.3 Heat treatment process for 17-4PH stainless steel

The heat treatment of experimental specimens was performed under the H900 HT condition, consisting of 2 processes: solution treatment (Solution HT), and aging treatment. A solution heat treatment was carried out at 1,038 °C (1,900 ºF) for 15-30 mins with subsequent air cooling, after which the solution treated samples were aged at 482 °C (900 ºF) for one hour and then air cooled (Sun *et al.*, 2018; Yoo, Lee, Youn, & Rhyim, 2006). Figure 2 shows (a) the H900 HT process's heat profile, and (b) the heat treatment furnace.

2.4 Microstructure characterization and mechanical testing

An optical microscope, Leica DM2500 M, was used to investigate the experimental specimen microstructures. The polished specimen was etched by Kalling's reagent acid including 50 ml of HCl, 50 ml of ethanol, and 2.5 g of $CuCl_2$ (Huber, Stich, & Fischer, 2022). The mechanical testing in this study included hardness and tensile tests. The hardness of specimens measured was the micro-Vickers hardness, with N.K. Testing HV-1000B, and an applied load of 100-gram force (gf) along the cross-section area of the specimen. Tensile tests were conducted by using SHIMDZU AGS-X 100 kN universal testing machine at room temperature with a strain rate of 0.00025 mm/(mm·sec). Figure 3 shows the tensile testing machine and the specimens. The tensile specimen dimensions were in accordance with the ASTM E8 standard methods for tension testing of metallic materials, as given in Figure 4 (a).

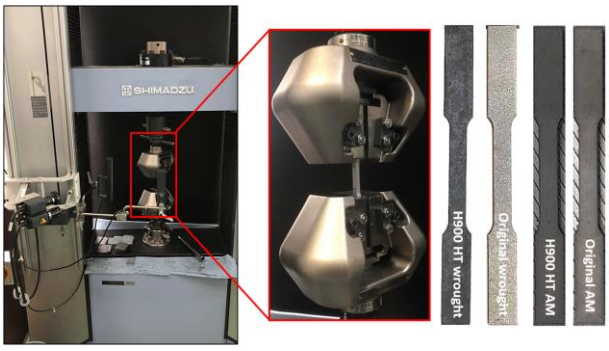

Figure 3. The tensile testing machine at Iron and Steel Institute of Thailand and the tensile test specimens

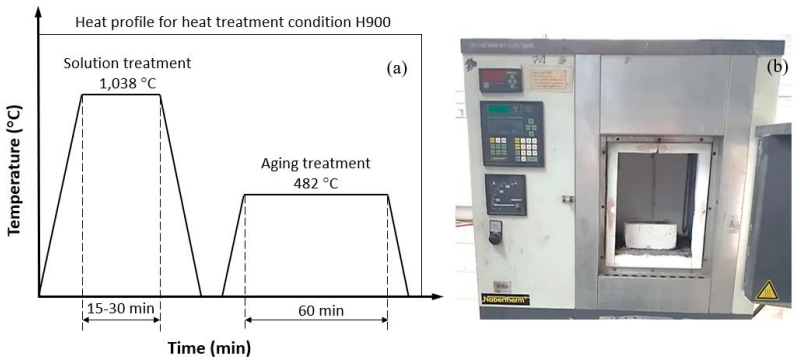

Figure 2. (a) H900 HT heat profile, and (b) the heat treatment furnace

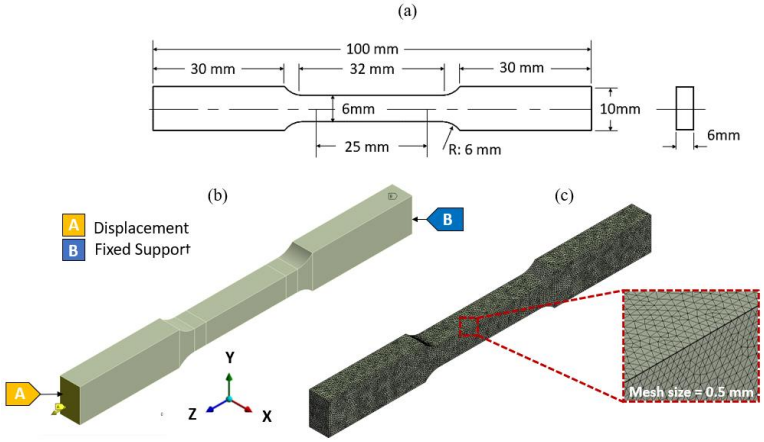

Figure 4. (a) Tensile specimen dimensions according to the ASTM E8 standard, (b) the fixed support and displacement regions of the test specimen, and (c) meshing of specimen

2.5 Computer simulation setup and mesh convergence analysis

The numerical simulation was performed by using the commercial software, ANSYS workbench 2020 R2. The input material properties employed in the simulation model were obtained from the mechanical properties and stress-strain curves of experimental materials, determined as mentioned in Section 3.3. Figure 4 (a) illustrates the tensile specimen dimensions according to the ASTM E8 standard. As shown in Figure 4 (b), the A region was set having displacement, while the B region was set as fixed support having zero displacement. The strain rate of 0.00025 mm/(mm·sec), defined by a displacement of 0.5 mm and end time of 80 seconds, was applied in this simulation. Figure 4 (c) presents the meshing of the CAD model. To gain a reliable simulation model and to assess the effect of the number of elements on the numerical results, a mesh convergence analysis was initially carried out in the study. The convergence by number of mesh elements was assessed by considering the maximum equivalent stress at gauge length area. As manifested in Figure 5, it was noted that the result from simulation model converged with the number of elements around 350,000, which was selected for the simulation model of the present study. After validation with experimental results, the strength coefficient (K) and strain hardening exponent (n) were used for prediction of the maximum force of bevel gear fabricated by MEAM process. The applied load on the part is in the maximum range that provides stress which does not exceed the yield point. Figure 6 shows boundary condition of AM bevel gear. The outside diameter and the inside diameter in the CAD model that was obtained from grabcad library are 35mm and 10 mm, respectively. The number of teeth is 20. The gear was discretized into 758,228 elements with 1,292,097 nodes.

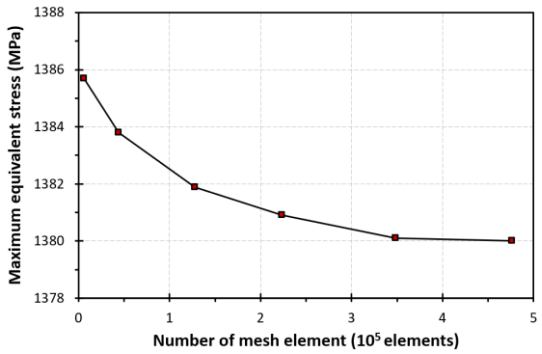

Figure 5. Mesh sensitivity analysis for numerical simulation model

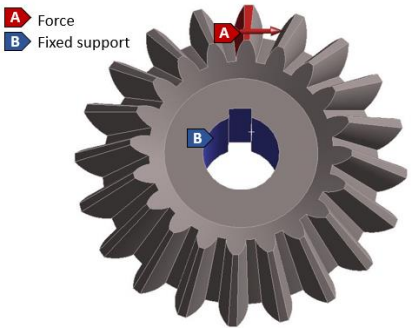

Figure 6. Boundary conditions of AM bevel gear

3. Results and Discussion

3.1 Microstructure

Microstructures of original and heat-treated AM and wrought 17-4PH stainless steel specimens are presented in Figure 7. The microstructures of original AM and wrought specimens comprised martensite and δ-ferrite as shown in Figures 7 (a) and (d), respectively. The AM specimen showed porosity after sintering. A similar result was shown in prior research studies (Huber *et al.*, 2022; Sabooni *et al.*, 2021; Sun *et al.*, 2018). After solution treatment of AM and wrought specimens, the δ-ferrite phase exhibited clear growth in martensite matrix as shown in Figures 7 (b) and (e). Subsequently, the aging treatment of AM and wrought parts was carried out. Figures 7 (c) and (f) show the microstructures of the specimens after aging. The microstructures obtained from the experiments are consistent with previous studies (Wu, Zhao, Wang, Wang, & Liang, 2018; Yoo *et al.*, 2006). In the precipitation during aging treatment, the abundant nucleation of Cu-rich clusters is responsible for the initial

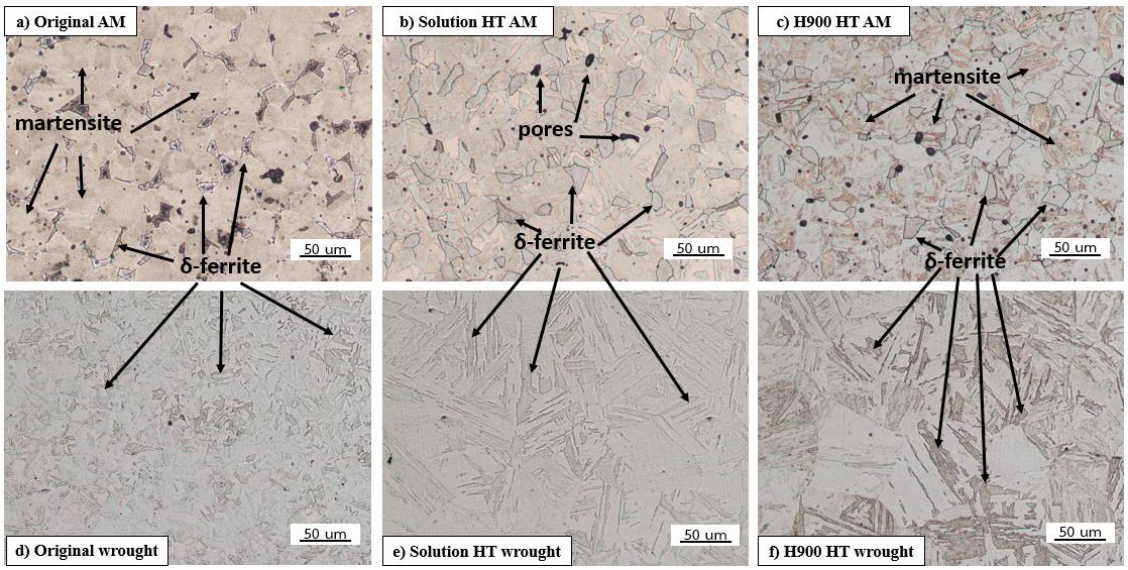

Figure 7. Optical micrographs showing microstructures of AM and wrought 17-4 PH stainless steels as (a, d) original, (b, e) after solution HT, and (c, f) after H900 HT

significant hardening effect in δ-ferrite (Wang, Li, Shen, Liu, & Wang., 2018), which provides a strengthening effect. The precipitation strengthening due to aging treatment was evidenced by the increases of tensile strength and hardness after H900 HT, as shown in Figure 8 and Table 3.

3.2 Micro-vickers hardness test

In this experiment, the micro-Vickers hardness was measured to evaluate the hardness of the specimens as original and after a heat treatment. The average hardness results shown in Table 3 are calculated from measured values at 15 testing points. It was found that the original and solution HT specimens of AM and wrought 17-4 PH stainless steels had analogous hardness values. The hardness values of H900 HT AM and wrought specimens increased due to the precipitation hardening from 318 to 414 HV for AM parts and from 349 to 483 HV for wrought parts, respectively. When comparing the hardness between AM and wrought part in the same state, it was found that the hardness of the wrought part was higher than that of the AM part, which was attributed to the porosity of the latter and the distribution characteristics of δ-ferrite phase.

3.3 Tensile test

Figure 8 (a) shows the engineering stress-strain curve of AM and wrought 17-4PH stainless steels as original and after heat treatment. The results of tensile test, as shown in Table 4, have the yield stress, Young's modulus, and ultimate tensile strength of both heat-treated specimens increased from the original ones. This is mainly due to the precipitation hardening of stainless steel in the H900 HT process. Both original specimens have greater elongation than the H900 HT specimens. The decrease in elongation with increasing tensile strength is a strength-ductility trade-off phenomenon that occurs with heat treatment, which in this research was with the H900 HT condition. Comparing the AM and wrought parts, both original and H900 HT specimens of AM parts show lesser elongation at break than the wrought parts, due to the porosity in the AM parts. Furthermore, the original AM specimen has tensile properties similar to the original MIM specimen (as stated in ASTM B833-05 standard) but with larger elongation.

Table 3. Microhardness of the original, solution HT, and H900 HT of 17-4PH AM and wrought specimen

	Microhardness (HV)	
	AM	Wrought
Original	318	349
Solution HT	321	358
H900 HT	414	483

The strength coefficient (K) and strain hardening exponent (n) in equation 1 are calculated from the true stress-strain curve, which is derived from the engineering stress-strain curve as shown in equations 2 and 3 (Callister & Rethwisch, 2017). Figure 8 (b) shows the true stress-strain curve of AM and wrought 17-4PH stainless steel as original and after heat treatment. The values of K and n for all specimens are summarized in Table 5. K-values are proportional to and influenced by ultimate tensile strength (UTS). The larger the UTS, the larger the K-value. The n-values of H900 HT of AM and wrought specimens are higher than those of the original specimens, due to the reduced elongation.

$$\sigma_{true} = K\varepsilon_{true}^{n} \quad (1)$$

$$\sigma_{true} = \sigma_{Eng}(1 + \varepsilon_{eng}) \quad (2)$$

$$\varepsilon_{true} = \ln(1 + \varepsilon_{eng}) \quad (3)$$

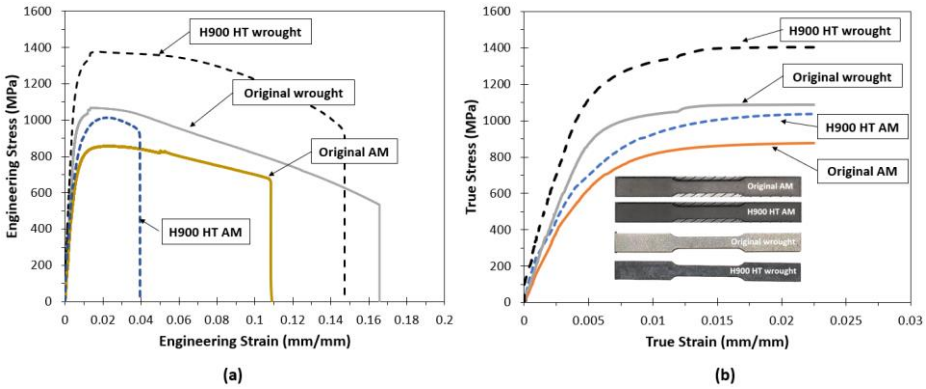

Figure 8. (a) Engineering and (b) true stress-strain curves of AM and wrought 17-4PH stainless steel in original condition and after heat treatment

Table 4. Tensile properties of original and heat treated (H900 HT) cases of AM, wrought, and MIM 17-4PH stainless steels

	Tensile properties			
	Yield stress (MPa)	Young's modulus (GPa)	Ultimate tensile strength (MPa)	Elongation (%)
Original AM	654	185	856	10.9
H900 HT AM	724	195	1,014	3.9
Original wrought	967	194	1,064	16.6
H900 HT wrought	1,231	231	1,378	14.7
Original MIM (ASTM B883-05)	650	190	795	4.0

Table 5. Strength coefficient and strain hardening exponent of original and H900 HT of 17-4PH stainless steel as AM and as wrought specimen

	Properties	
	Strength coefficient, K (MPa)	Strain hardening exponent, n
Original AM	1,291	0.099
H900 HT AM	1,768	0.137
Original wrought	1,803	0.123
H900 HT wrought	2,617	0.149

3.4 Simulation results and experiment validation

The tensile properties including K and n values obtained experimentally in section 3.3 were used as input data in the simulation. Figure 9 represents the validation between the simulation and the experimental results of the true stress-strain curve and true strain with applied stress of 600 MPa for all specimens. The validation results show good agreement between the simulation and experimental findings. The stress of 600 MPa was applied in this study to analyze the strain in elastic region, as this value does not exceed the yield stress. The true strains of AM and wrought part are 5.91×10^{-3} and 3.27×10^{-3} mm/mm for original specimen and 4.44×10^{-3} and 2.83×10^{-3} mm/mm for H900 HT specimen. The AM part has larger strain in the elastic region than the wrought part due to its lower hardness and Young's modulus.

In addition, the simulation results show that for the specimens as original and H900 HT, respectively, the maximum applied forces on the bevel gear created by the MEAM process that deliver stress not greater than the yield point were 2,500 and 3,900 kN. Figure 10 depicts the simulation results of stress distribution in the AM bevel gear.

4. Conclusions

In this study, comparisons of microstructure and mechanical properties between AM and wrought 17-4PH stainless steels as original and after heat treatment were performed. Both experimental and numerically simulated tensile testing of the stainless steel were also carried out to acquire the K and n values of the material, in order to then predict the mechanical properties of the AM parts fabricated by MEAM process. The main results obtained from the study can be summarized as follows:

1. The microstructures of the original AM and wrought specimen comprised martensite and δ-ferrite. The AM specimen was porous. In solution HT, the δ-ferrite phase expanded in the martensite matrix. After aging, the H900 HT specimens showed increased hardness and tensile strength due to the precipitation strengthening effect of Cu-rich δ-ferrite phase. Although the original AM specimen had larger elongation, its tensile properties were similar to those of the original MIM specimen.
2. The simulated true stress-strain curves for all specimens were consistent with the experimental results. When comparing the AM and the wrought parts, the elongation of the AM part in the elastic region (at $\sigma = 600$ MPa) is greater than of the wrought part due to the

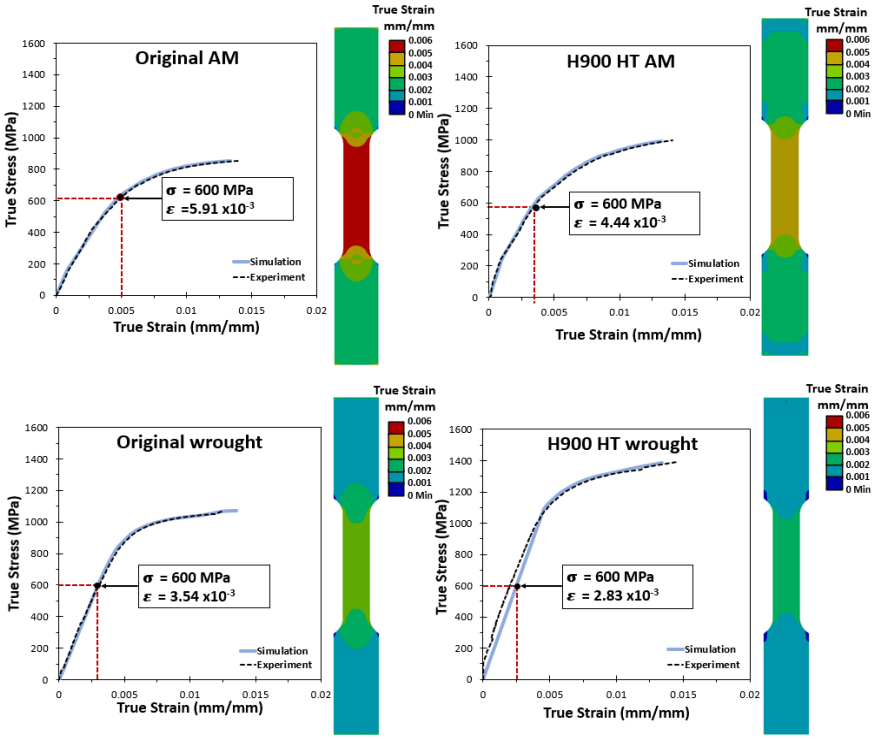

Figure 9. The validation between numerical simulation and experimental results of the true stress-strain curve and the true strain with applied stress of 600 MPa for all specimens

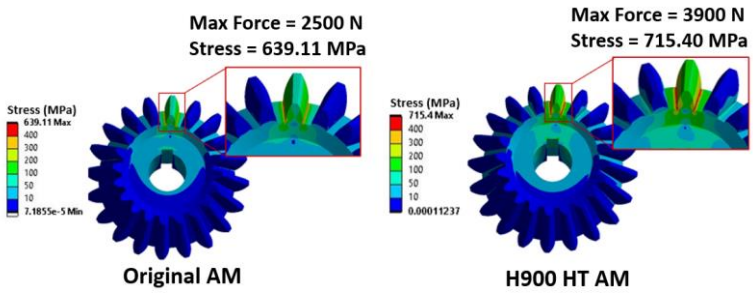

Figure 10. The stress distribution caused by the maximum applied force that does not exceed the yield stress in AM bevel gear as original and H900 HT.

lower hardness and Young's modulus of AM parts. In contrast, the elongation at fracture point of the AM part is lower than that of the wrought part due to porosity of the AM part.

3. After validation with experimental results, one simulation case study of the applied load on the AM bevel gear was presented. For the specimens as original and H900 HT, the maximum applied forces on the bevel gear fabricated by the MEAM process that provide stresses not exceeding the yield point are 2,500 and 3,900 kN, respectively.

Acknowledgements

This research was funded by Thailand Science Research and Innovation Fund, and King Mongkut's University of Technology North Bangkok with contract no. KMUTNB-65-FF-48; Thailand Graduate Institute of Science and Technology (TGIST), National Science and Technology Development Agency (NSTDA) with contract no. SCA-CO-2563-12109-TH; Innovation and technology assistance program, (iTAP, NSTDA) and Thaisakol Group Co., Ltd.

References

Abe, Y., Kurose, T., Santos, M. V. A., Kanaya, Y., Ishigami, A., Tanaka, S., & Ito, H. (2021). Effect of layer directions on internal structures and tensile properties of 17-4PH stainless steel parts fabricated by fused deposition of metals. *Materials*, *14*, 1-12. doi:10.3390/ma14020243

ASTM International. (2005). *ASTM B883-05, Standard specification for metal injection molding (MIM) ferrous materials*. West Conshohocken, PA: Author.

Callister, W. D., & Rethwisch, J. D. G. (2017). *Materials science and engineering: An introduction* (10th ed). Hoboken, NJ: John Wiley and Sons.

Chen, Y., Clark, S. J., Sinclair, L., Leung, C. L. A., Marussi, S., Connolley, T., . . . Lee, P. D. (2021). Synchrotron X-ray imaging of directed energy deposition additive manufacturing of titanium alloy Ti-6242. *Additive Manufacturing*, *41*, 1-9. doi:10.1016/j.addma.2021.101969

Farshidianfar, M. H., Khodabakhshi, F., Khajepour, A., & Gerlich, A. P. (2021). Closed-loop control of microstructure and mechanical properties in additive manufacturing by directed energy deposition. *Materials Science and Engineering*, *803*, 1-16. doi:10.1016/j.msea.2020.140483

Gorunov, A. I. (2020). Additive manufacturing of Ti6Al4V parts using ultrasonic assisted direct energy deposition. *Journal of Manufacturing Processes*, *59*, 545-556. doi:10.1016/j.jmapro.2020.10.024

Haley, J. C., Zheng, B., Bertoli, U. S., Dupuy, A. D., Schoenung, J. M., & Lavernia, E. J. (2016). Working distance passive stability in laser directed energy deposition additive manufacturing. *Materials and Design*, *161*, 86–94. doi:10.1016/j.matdes.2018.11.021

Heigel, J.C., Michaleris, P., & Reutzel, E.W. (2015). Thermo-mechanical model development and validation of directed energy deposition additive manufacturing of Ti–6Al–4V. *Additive Manufacturing*, *5*, 9–19. doi:1016/j.addma.2014.10.003

Herzog, D., Seyda, V., Wycisk, E., & Emmelmann, C. (2016). Additive manufacturing of metals. *Acta Materialia*, *117*, 371-392. doi:10.1016/j.actamat.2016.07.019

Huber, D., Stich, P., & Fischer A. (2022). Heat treatment of 17–4 PH stainless steel produced by binder jet additive manufacturing (BJAM) from N2-atomized powder. *Progress in Additive Manufacturing*, *7*, 187–199. doi:10.1007/s40964-021-00224-z

Kumaran, M., Senthilkumar, V., Panicke, C. T. J., & Shishir, R. (2021). Investigating the residual stress in additive manufacturing of repair work by directed energy deposition process on SS316L hot rolled steel substrate. *Materials Today: Proceedings*, *47* (14), 4475-4478. doi:10.1016/j.matpr.2021.05.319

Kurose, T., Abe, Y., Santos, M. V. A., Kanaya, Y., Ishigami A., Tanaka, S., & Ito, H. (2020). Influence of the layer directions on the properties of 316L stainless steel parts fabricated through fused deposition of metals. *Materials*, *13*, 1-12. doi:10.3390/ma13112493

Li, K., Zhan, J., Yang, T., To, A. C., Tan, S., Tang, Q., . . . Murr, L. E. Homogenization timing effect on microstructure and precipitation strengthening of 17–4PH stainless steel fabricated by laser powder bed fusion. *Additive Manufacturing*, *52*, 1-17. doi:10.1016/j.addma.2022.102672

Meenashisundaram, G. K., Xu, Z., Nai, M. L. S., Lu, S., Ten, J. S., & Wei, J. (2020). Binder Jetting Additive Manufacturing of High Porosity 316L Stainless Steel Metal Foams. *Materials*, *13*(3744), 1-23. doi:10.3390/ma13173744

Milner, B. B., Gradl, P., Snedden, G., Brooks, M., Pitot, J., Lopez, M., . . . Plessis, A. D., (2021). Metal additive manufacturing in aerospace: A review. *Materials and Design*, *209*, 1-33. doi:10.1016/j.matdes.2021.110008

Mirzababaei, S., Paul, B., & Pasebani, S. (2020). Metal Powder Recyclability in Binder Jet Additive Manufacturing. *Metals and Materials Society*, *72*(9), 1-10. doi:10.1007/s11837-020-04258-6

Mussatto, A., Groarke, R., Vijayaraghavan, R. K., Obeidi, M. A., McNally, P. J., Nicolosi, V., . . . Brabazon, D. (2022). Laser-powder bed fusion of silicon carbide reinforced 316L stainless steel using a sinusoidal laser scanning strategy. *Journal of Materials Research and Technology*, *18*, 2672-2698. doi:10.1016/j.jmrt.2022.03.170

Nandwana, P., Kannan, R., & Siddel, D. (2021). Micro structure evolution during binder jet additive manufacturing of H13 tool steel. *Additive Manufacturing*, *36*, 1-11. doi:10.1016/j.addma.2020.101534

Ninpetch, P., Chalermkarnnon, P., & Kowitwarangkul, P. (2022). Multiphysics simulation of thermal-fluid behavior in laser powder bed fusion of H13 steel: Influence of layer thickness and energy input. *Metals and Materials International*, *205*, 1-16. doi:10.1007/s12540-022-01239-z

Ninpetch, P., Kowitwarangkul, P., Chalermkarnnon, P., Promoppatum, P., Chuchuay, P. & Rattanadecho, P. (2022). Numerical modeling of distortion of Ti-6Al-4V components manufactured using laser powder bed fusion. *Metals*, *12*(1484), 1-15. doi:10.3390/met12091484

Ninpetch, P., Kowitwarangkul, P., Mahathanabodee, S., Chalermkarnnon, P., & Rattanadecho, P. (2021). Computational investigation of thermal behavior and molten metal flow with moving laser heat source for selective laser melting process. *Case Studies in Thermal Engineering*, *24*, 1-10. doi:10.1016/j.csite.2021.100860

Ninpetch, P., Kowitwarangkul, P., Mahathanabodee, S., Chalermkarnnon, P., & Ratanadecho, P. (2020). A review of computer simulations of metal 3D printing. *AIP Conference Proceedings*, *2279*, 1-25. doi:10.1063/5.0022974

Oropeza, D., & Hart, A. J. (2021). A laboratory-scale binder jet additive manufacturing testbed for process exploration and material development. *Journal of Advanced Manufacturing Technology*, *114*, 3459-3473. doi:10.1007/s00170-021-07123-1

Pagac, M., Hajnys, J., Halama, R., Aldabash, T., Mesicek, J., Jancar, L., & Jansa, J. (2021). Prediction of model distortion by FEM in 3D printing via the selective laser melting of stainless steel AISI 316L. *Applied sciences*, *11*(1656), 1-12. doi:10.3390/app110416 56

Pant, M., Nagdeve, L., Kumar, H., & d Moona, G. (2022). A contemporary investigation of metal additive manufacturing techniques. *Sādhanā, 47, 18,* 1-19. doi:10.1007/s12046-021-01770-6

Pitrmuc, Z., Beranek, J. S. L., Mikes, P., Andronov, V., Sommer, J., & Holesovsky, F. (2022). Mechanical

and Microstructural Anisotropy of Laser Powder Bed Fusion 316L Stainless Steel. *Materials*, *15*(551), 1-12. doi:10.3390/ma15020551

Sabooni, S., Chabok, A., Feng, S. C., Blaauw, H., Pijper, T. C., Yang, H. J. & Pei, Y. T. (2021). Laser powder bed fusion of 17–4 PH stainless steel: A comparative study on the effect of heat treatment on the microstructure evolution and mechanical properties. *Additive Manufacturing*, *46*, 1-10. doi:10.1016/ j.addma.2021.102176

Saboori, A., Aversa, A., Bosio, F., Bassini, E., Librera, E., Chirico, M. D., . . . Lombardi, M. An investigation on the effect of powder recycling on the microstructure and mechanical properties of AISI 316L produced by Directed Energy Deposition. *Materials Science and Engineering*, *766*, 1-11. doi:10.1016/j.msea.2019.138360

Sookchanchai, K., Promoppatum, P., & Uthaisangsuk, V. (2022). Load-carrying capacity of additively manufactured part using graded-topology infilled lattices structures. *Mechanics of Advanced Materials and Structures*, *1*, 1-19. doi:10.1080/ 15376494.2022.2135145

Sun, Y., Hebert, R. J., & Aindow, M. (2018). Effect of heat treatments on microstructural evolution of additively manufactured and wrought 17-4PH stainless steel. *Materials and Design*, *156*, 429-440. doi:10.1016/j.matdes.2018.07.015

Wang, Z., Li, H., Shen, Q., Liu, W., & Wang, Z. (2018). Nano-precipitates evolution and their effects on mechanical properties of 17-4 precipitation-hardening stainless steel. *Acta Materialia*, *156*, 158-171. doi:10.1016/j.actamat.2018.06.031

Wheat, E., Vlasea, M., Hinebaugh, J., & Metcalfe, C. (2018). Sinter structure analysis of titanium structures fabricated via binder jetting additive manufacturing. *Materials and Design*, *156*, 167–183. doi:10. 1016/j.matdes.2018.06.038

Wu, M., Zhao, Z., Wang, X., Wang, C., & Liang, P. (2018). Corrosion behavior of 17–4 PH stainless steel in simulated marine environment. *Materials and Corrosion*, *1*, 1-9. doi:10.1002/maco.201810454

Yoo, W. D., Lee, J. H., Youn, K. T., & Rhyim, Y. M. (2006). Study on the Microstructure and Mechanical Properties of 17-4 PH Stainless Steel depending on Heat Treatment and Aging Time. *Solid State Phenomena*, *118*, 15-20. doi:10.4028/www. scientific.net/SSP.118.15

Zhang, K., Zhang, W., Brune, R., Herderick, E., Zhang, X., Cornell, J., & Forsmark, J. (2021). Numerical simulation and experimental measurement of pressureless sintering of stainless-steel part printed by Binder Jetting Additive Manufacturing. *Additive Manufacturing*, *47*, 1-18. doi:10.1016/j.addma. 2021.102330

Zhang, Q., Xie, J., London, T., Griffiths, D., Bhamji, I., & Oancea, V. (2019). Estimates of the mechanical properties of laser powder bed fusion Ti-6Al-4V parts using finite element models. *Materials and Design*, *169*, 1-11. doi:10.1016/j.matdes.2019.1076 78